AIAA SciTech Forum
23-27 January 2023, National Harbor, MD & Online
AIAA SCITECH 2023 Forum

10.2514/6.2023-0658

Study of Separation Control Using Pulsed Co-Flow Jet and Its Energy Expenditure

Kewei Xu *, Gecheng Zha †
Dept. of Mechanical and Aerospace Engineering
University of Miami, Coral Gables, Florida 33124
E-mail: gzha@miami.edu

Abstract

This paper numerically studies the control effectiveness and energy expenditure of pulsed Co-Flow Jet (PCFJ) applied on the widely used NASA hump. The 2D unsteady Reynolds averaged Navier-Stokes equations are solved for the simulations. An unsteady velocity boundary condition is developed for the in-house FASIP (Flow-Acoustics-Structure Interaction Package) CFD solver to simulate the pulsed CFJ. The pulsed jet simulation is validated with the NASA tested case actuated by a synthetic jet for the NASA hump flows. The predicted synthetic jet results are in good agreement with the experiment in terms of pressure coefficient (C_p) distributions. For the pulsed CFJ, a novel actuation model with continuous suction and pulsed injection is proposed to mimic the zero-net-mass-flux pulsing process and calculate the power consumption. The pulsed CFJ and steady CFJ (SCFJ) are compared for their control effectiveness and power consumption at their minimum momentum coefficient (C_μ) to fully attach the flow. The pulsed CFJ is simulated with two reduced frequencies (F^+) of 0.74 and 1.67. All the cases have identical CFJ injection and suction slot locations and sizes. Results show that the steady and pulsed CFJ cases have the similar control effectiveness as their C_p distributions are virtually overlapped. The PCFJ requires about 28% lower mass flow rate than that of the SCFJ. However, the PCFJ requires substantially higher power consumption due to significantly increased total pressure loss for pulsed jet actuation.

Nomenclature

AoA	Angle of attack
AFC	Active flow control
C	Hump chord length
CFJ	Co-flow jet
c_p	Constant pressure specific heat
C_p	Pressure coefficient, $(P - P_\infty)/(\frac{1}{2}\rho_\infty U_\infty^2)$
C_μ	Jet momentum coefficient, $\dot{m}_j V_j/(\frac{1}{2}\rho_\infty U_\infty^2 S)$
F^+	Reduced frequency, $f * C/U_\infty$
LE	Leading edge
$\dot{m}$	Mass flow
Ma	Mach number
$\dot{m}$	Mass flow rate
$\overline{\dot{m}}$	Non-dimensional mass flow rate, $\dot{m}/(U_\infty \rho_\infty S)$

* Ph.D. Student
† Professor, ASME Fellow, AIAA associate Fellow

P	CFJ Pumping power
P_c	Power coefficient, $P/(\frac{1}{2}\rho_\infty U_\infty^3 S)$
$RANS$	Reynolds-Averaged Navier-Stokes
Re	Reynolds number
TE	Trailing edge
$ZNMF$	Zero-net mass flux
c	Subscript, stands for corrected
j	Subscript, stands for jet
0	Subscript, stands for total
γ	Air specific heats ratio
Γ	Total pressure ratio
η	Micro-compressor efficiency

1 Introduction

Active Flow Control (AFC) has the potential to break through conventional fluid mechanics limitations and provides significant performance improvement to fluid systems [1]. AFC is to transfer external energy to the controlled flow in order to improve the performance of the flow system. Prandtl's rotating cylinder experiment in 1934 was one of the earliest AFC studies to transfer mechanical energy to flow via the surface shear stress of a rotating cylinder [2]. However, systematic studies of AFC have only occurred recently due to more and more challenging applications of flow systems.

For all AFC systems, there are three measures of merit (MoM): 1) effectiveness; 2) power required (PR); and 3) power conversion efficiency (PCE). Effectiveness quantifies the performance enhancement, e.g., removal of flow separation, drag reduction, lift increase, stall prevention, noise mitigation, etc. Power required quantifies the AFC power needed to achieve the targeted effectiveness. Power conversion efficiency quantifies the efficiency to convert the external power (e.g., mechanical, electric, chemical) to the power required by the controlled flow. It determines how much total power will be consumed by the actual flow control system.

For an AFC to benefit industry realistic applications, all three MoM matter. The ultimate criterion for an AFC is that the system efficiency gain should be greater than the AFC energy expenditure. However, the current AFCs do not always have clear quantification of all the MoM, in particular for the PR and PCE, partially because they may not always be easy to measure. For a zero-net-mass-flux (ZNMF) flow control, it is more straightforward to measure the PR and PCE because it is a closed system. For a non-ZNMF flow control such as the one using injection-only, namely an open system, the PR is difficult to measure because it depends on the path that the mass flow source is supplied. The PCE measurement could be even more difficult because it also depends on the actuators used and their integration with the system (e.g. aircraft). Similarly, for the flow control with suction-only, the PR and PCE depend on the path that the flow is discharged to the sink. In other words, the PR and PCE of the non-ZNMF flow control are path-dependent. A long path, in general, will suffer from a high energy loss, in particular, if the path requires a flow turning perpendicular to the controlled flow plane.

Synthetic jets [3, 4, 5, 6, 7, 8] generated by the periodic motion of a piston or diagram and plasma jets based on plasma discharge [9, 10, 11, 12, 13] are zero-net-mass-flux flow controls, which require no external flow source. However, both the synthetic and plasma jets, in general, provide low input momentum due to low energy conversion efficiency from electric to fluid power, typically 3% $\sim$ 10% [14, 15, 16] for synthetic jets and less than 1% for plasma actuators [17]. The control effectiveness of synthetic and plasma jets is thus limited for high momentum flows.

The flow control methods using fluidic actuators generally can provide high momentum with a high control authority. An example is the widely used circulation control (CC) relying on jet injection and Coanda effect [18, 19, 20, 21]. A CC airfoil is effective to enhance lift coefficient. However, CC airfoil is an injection-only flow control method. The PR is path-dependent and a systematic study of PR for CC airfoil is not well documented in published literature.

Pulsed fluidic jets attract a lot of interest [22, 23, 24, 25, 26, 27, 28, 29, 30, 31, 32] as they are able to achieve the same control effectiveness of a steady jet with lower injection momentum coefficient and mass flow. This is important for the non-ZNMF flow control such as the CC flow control that may introduce the mass flow from an air-breathing engine. Minimizing the engine bleed mass flow is desirable for the overall engine system efficiency. Pulsed jet is considered to have the advantage to enhance mixing due to the excited large vortex structures [22, 23, 24, 25, 26].

However, few studies are conducted to address an important question: does the reduced mass flow of the pulsed jet brings the advantage of reduced the energy consumption compared with the steady jet? The answer is not obvious since a fluidic actuator power consumption is determined linearly by the mass flow rate and exponentially by the required total pressure ratio. Lacking study on this question can be again attributed to the flow path dependence issue previously mentioned. For the pulsed jet, it is even more unclear how to quantify the power consumption, which is related to the jet mass supply process. In laboratory studies, the flow supply is often introduced from a large high-pressure reservoir. The dynamic flow process or flow path is usually not the focus and is rarely studied, in particular for the injection-only flow control. For a zero-net-mass-flux (ZNMF) fluidic flow control system, the dynamic pulsed jet flow path needs to be considered to evaluate the power consumption.

Among various fluidic AFC techniques, Co-flow Jet is a zero-net mass-flux (ZNMF) flow control method recently developed by Zha et al. [33, 34, 35, 36, 37, 38, 39, 40, 41, 42, 43]. It is demonstrated numerically and experimentally that CFJ achieves significant improvements on airfoil lift augmentation, drag reduction, and stall margin enlargement. In a CFJ airfoil, electric micro-compressors [44, 45] along with suction and injection ducts are embedded inside the airfoil as shown in Fig. 1. The micro-compressor works as an actuator that draws flow near the trailing edge (TE), pressurizes the flow, and ejects it as a jet near the leading edge (LE).

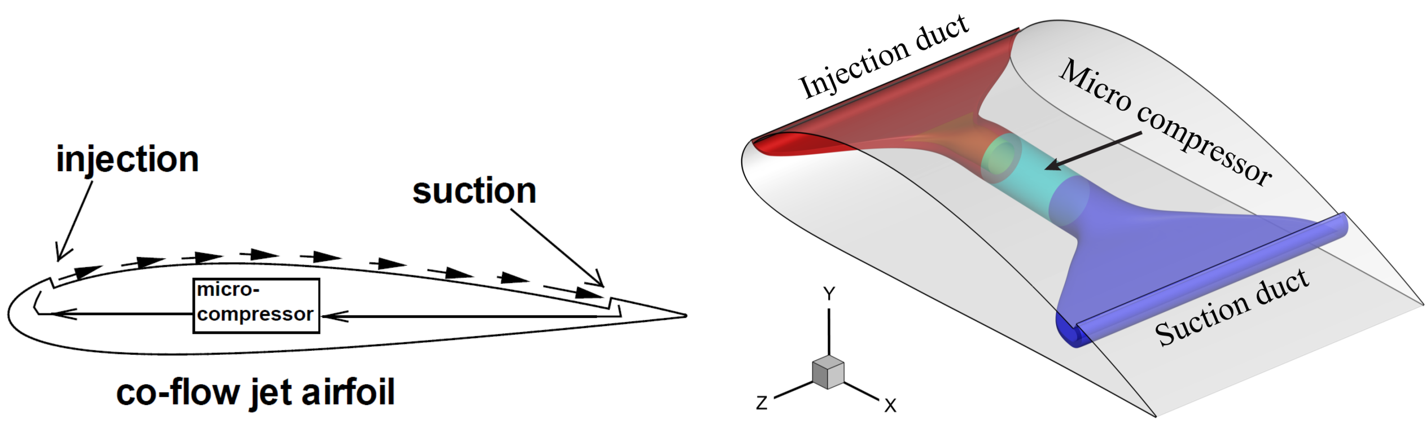

(a) 2D CFJ airfoil (b) 3D wing

Figure 1: Schematics of the CFJ airfoil and wing.

The purpose of this paper is two-fold: 1) develop a model to calculate the power consumption of pulsed co-flow jet, which is not studied so far. 2) Using the NASA hump as an example to numerically study and compare the performance of pulsed CFJ (PCFJ) and steady CFJ (SCFJ), in particular, to understand their energy consumption.

2 Numerical Approaches

2.1 Governing Equations

The governing equations for the CFD simulation are the unsteady Reynolds averaged Navier-Stokes equations (URANS) with one equation Spalart-Allmaras turbulence model [46], which are solved in a fully coupled manner using an implicit unfactored Gauss-Seidel line iteration to achieve a high convergence rate [47]. The normalized Navier-Stokes governing equations in generalized coordinates are expressed below:

$$\frac{\partial \mathbf{Q}}{\partial t}+\frac{\partial \mathbf{E}}{\partial \xi}+\frac{\partial \mathbf{F}}{\partial \eta}+\frac{\partial \mathbf{G}}{\partial \zeta}=\frac{1}{Re}\left[\frac{\partial \mathbf{R}}{\partial \xi}+\frac{\partial \mathbf{S}}{\partial \eta}+\frac{\partial \mathbf{T}}{\partial \zeta}\right]+\mathbf{S}_\nu \tag{1}$$

where Re is the Reynolds number. The conservative variable vector $\mathbf{Q}$, inviscid flux $\mathbf{E}$, viscous flux vector $\mathbf{R}$ are given below, and the rest can be expressed following the symmetric rule.

$$\mathbf{Q}=\frac{1}{J}\begin{bmatrix}\rho\\ \rho u\\ \rho v\\ \rho w\\ \rho e\\ \rho\hat{\nu}\end{bmatrix},\ \mathbf{E}=\frac{1}{J}\begin{bmatrix}\rho U\\ \rho uU+p\xi_x\\ \rho vU+p\xi_y\\ \rho wU+p\xi_z\\ (\rho e+p)U\\ \rho\hat{\nu}U\end{bmatrix},\ \mathbf{R}=\frac{1}{J}\begin{bmatrix}0\\ \tau_{xi}\xi_i\\ \tau_{yi}\xi_i\\ \tau_{zi}\xi_i\\ (u_j\tau_{ij}-q_i)\xi_i\\ \frac{\rho}{\sigma}(\nu+\hat{\nu})\frac{\partial\hat{\nu}}{\partial x_i}\xi_i\end{bmatrix},\ \mathbf{S}_\nu=\begin{bmatrix}0\\0\\0\\0\\0\\S_\nu\end{bmatrix}$$

The $\mathbf{S}_\nu$ in Eq. (1) is the source term for the S-A model,

$$\begin{aligned}S_\nu=&\frac{1}{J}\left[\frac{1}{Re}\left[-\rho\left(c_{w1}f_w-\frac{c_{b1}}{\kappa^2}f_{t2}\right)\left(\frac{\tilde{\nu}}{d}\right)^2\right]\right.\\&\left.+\frac{1}{Re}\left[\frac{\rho}{\sigma}c_{b2}\left(\nabla\tilde{\nu}\right)^2-\frac{1}{\sigma}\left(\nu+\tilde{\nu}\right)\nabla\tilde{\nu}\bullet\nabla\rho\right]+Re\left[\rho f_{t1}\left(\Delta q\right)^2\right]+\rho c_{b1}\left(1-f_{t2}\right)\tilde{S}\tilde{\nu}\right]\end{aligned} \tag{2}$$

Other auxiliary relations and coefficients for the S-A turbulence model can be found in [48, 46].

2.2 Navier-Stokes Equations Solver

The in-house high order CFD code FASIP (Flow-Acoustics-Structure Interaction Package) is used to solve the 2D URANS equations. A 3rd order WENO scheme for the inviscid flux [47, 49, 50, 51, 52, 53] and 4th order central differencing for the viscous terms [49, 53] is employed to discretize the Navier-Stokes equations. The low diffusion E-CUSP scheme suggested by Zha et al [50] based on the Zha-Bilgen flux vector splitting [54] is utilized with the WENO scheme to evaluate the inviscid fluxes. All the simulations in this study are conducted as unsteady time-accurate simulations. The second order time accurate implicit method with pseudo time and Gauss-Seidel line relaxation is used to achieve a fast convergence rate [47, 55]. Parallel computing is implemented to save wall clock simulation time [55, 56]. The numerical results are time-averaged results after the flows and all the aerodynamic forces become dynamically stable. The FASIP code is intensively validated for CFJ simulations

[35, 37, 38, 39, 40, 41, 42, 56, 57, 58]. Particularly, the predicted power coefficient P_c of CFJ agrees very well with the experiment [40], which provides a solid support for the energy prediction in the present study.

For the synthetic jet simulation as a validation, an unsteady velocity inlet boundary condition is employed for the subsonic pulsed injection jets. The velocity is specified to be normal to the inlet boundary surface with a sinusoidal function defined by Eq. (3), where V_{peak} is the peak velocity of the synthetic jet and ω is the angular frequency. Two velocity components u and v are thus determined. The static pressure p on the inlet boundary is extrapolated from the inner domain. For the pulsed co-flow jet, the velocity boundary is specified in the same manner, but in a square wave function. During the CFJ-on duty period, $V(t)$ is set to be a specified constant value. During the CFJ-off period, $V(t)$ is set to be 0.

$$V(t) = V_{peak} sin(\omega t) \tag{3}$$

3 Numerical Validation

3.1 NASA Hump Geometry

The NASA hump is widely used as a benchmark case to validate numerical algorithms and turbulence modeling [59] for flow control. The baseline hump configuration with no flow control is designed to have a converging section followed by a rapid area expansion downstream of the throat as shown in Fig. 2, which creates a severe diffusion and large flow separation.

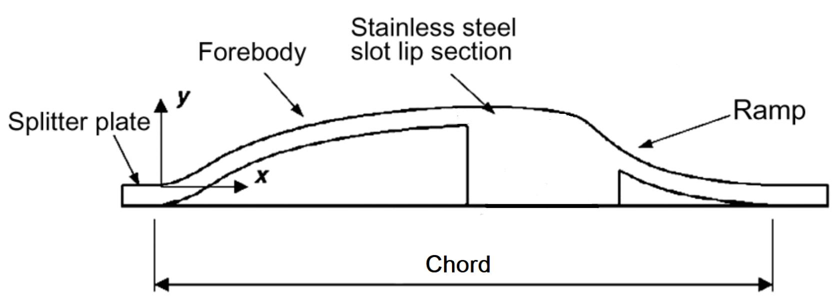

Figure 2: Geometry of the hump upper surface [60].

3.2 Baseline Hump with no Flow Control

The flow of the baseline hump is simulated with an initial mesh size of 408×108 in the stream-wise and transverse direction, respectively. The mesh topology and boundary conditions used by Ramsey [59] are adopted [61]. Fig. 3 (a) is the Mach number contours displaying a large flow separation downstream of the baseline hump. Fig. 3 (b) gives the corresponding C_p and $\partial p/\partial x$ distributions of the viscous results. The present numerical simulation is in very good agreement with the experiment for the C_p distribution and separation onset location at x/C=66.3%. The measured onset point in the experiment is at 66.5%C. The predicted separation onset location is determined using the skin friction distribution [61]. The mesh refinement study is also conducted by doubling the grid points in both directions. The reattachment point is slightly over-predicted as reported by other research groups using RANS models [59, 62]. The mesh refinement study indicates that the solutions are converged based on the initial mesh size. The unsteady simulation uses a constant non-dimensional characteristic time step $\Delta\bar{t} = 5\times10^{-3}$ with the maximum L2-norm residual typically reduced by 2 orders of magnitude within less than 40 pseudo time iterations per physical time step. Details of the residual convergence histories are presented in Ref. [61].

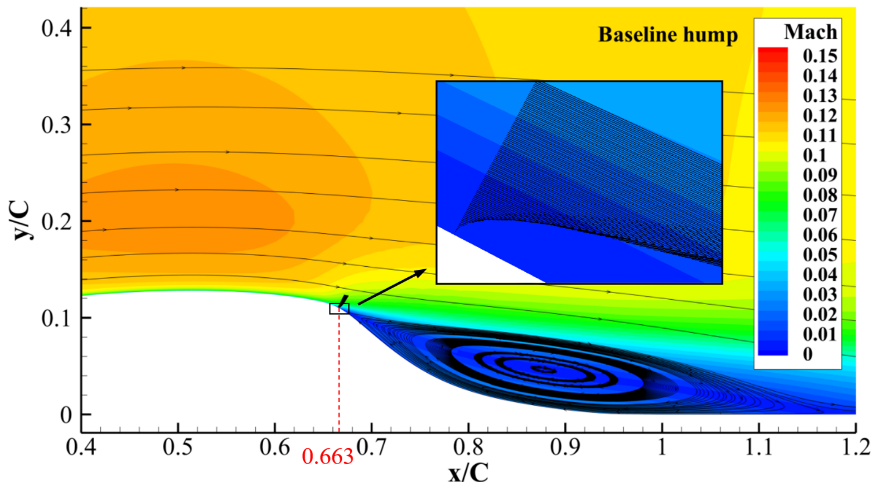

(a) Mach number contours

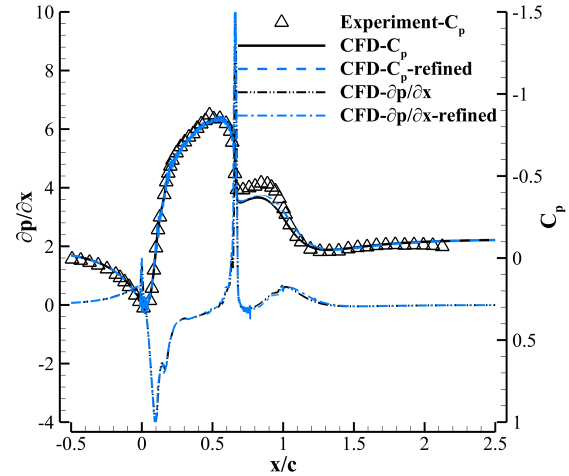

(b)$\partial p/\partial x$ and C_p distributions

Figure 3: Results of the viscous baseline hump.

3.3 The Hump with a Synthetic Jet

The pulsed jet simulation is validated in this section with the synthetic jet experiment conducted for the NASA hump: CFDVAL2004 Case 3 [59]. The synthetic jet is located at x/C=0.65 with the jet slot zoomed in Fig. 6 (a). The case has the excitation frequency (f) of 138.5 Hz, peak blowing velocity (V_{peak}) of 27 m/s, and averaged C_μ of 0.11%. Fig. 4 shows the time history of the unsteady injection velocity normalized by the free-stream velocity. It has the same frequency and peak blowing velocity as the experimental measurement [59]. Fig. 5 is the instantaneous pressure contours of the hump flow actuated by synthetic jet, which shows that the pressure waves propagate upstream and downstream of the jet slot. Fig. 6 (a) shows the computed time-averaged Mach number contours of the NASA hump flow with synthetic jet. The unsteady velocity boundary condition is applied near the jet exit as shown in the zoomed-in view. The Mach contours show that the synthetic jet with the given strength is not able to attach the flow. Fig. 6 (b) compares the C_p distributions between the predicted and tested cases. The predicted C_p overlaps with tested data in most of the locations except at $0.7 < x/C < 1.2$, which is due to the limitation of URANS to resolve the separated flow. The mesh refinement studies shown in Fig. 6 (b) do not change the calculated results, indicating that the solutions achieve mesh independence.

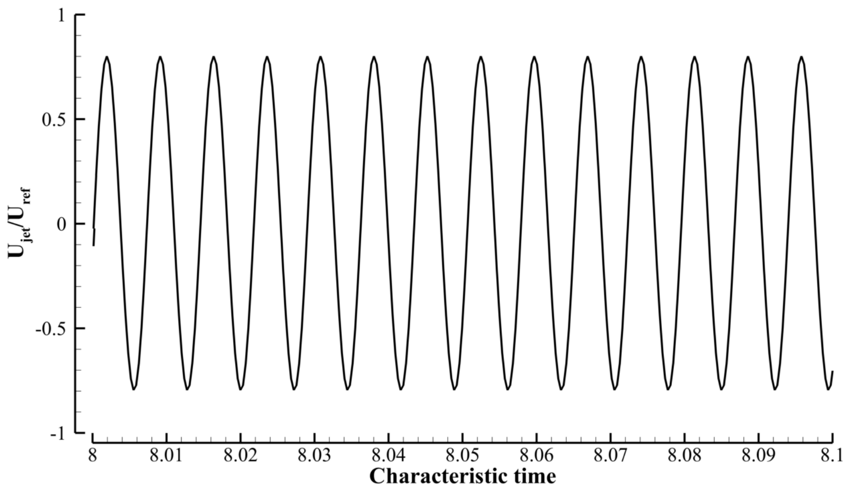

Figure 4: Time history of the unsteady synthetic jet velocity boundary, normalized by free-stream velocity

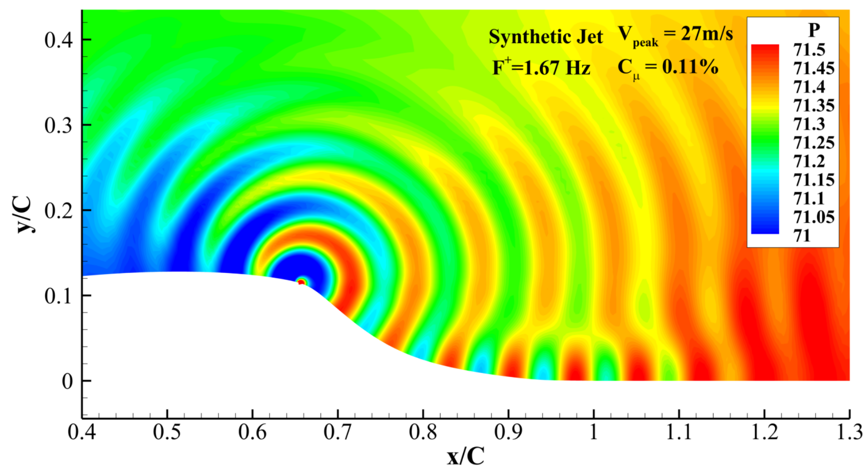

Figure 5: Instantaneous normalized pressure contours of the hump actuated by synthetic jet ($\bar{t}$=13.357)

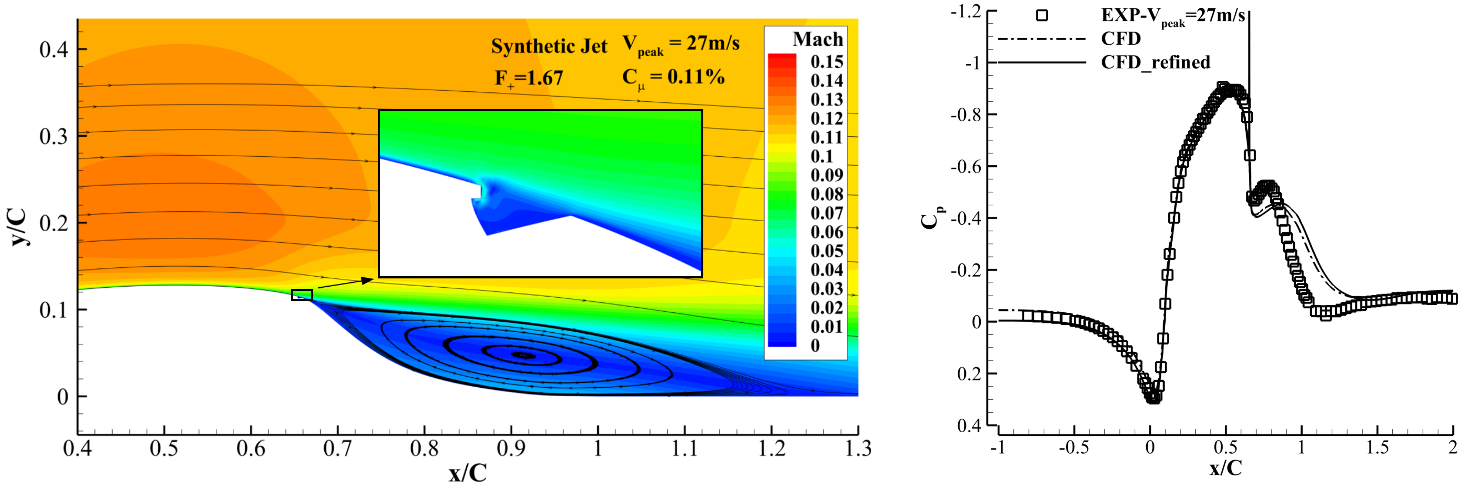

(a) Time-averaged Mach number contours (b) Time-averaged C_p distributions, F^+=1.67

Figure 6: Results of the hump flow with synthetic jet.

4 Pulsed Co-flow Jet Flow Process Model

To develop a model evaluating the power of PCFJ, we need to first develop a model to describe the PCFJ flow process. Since the flow must satisfy mass conservation, the suction process to supply the mass flow must be included. There may be two models: A) Pulsed injection with a continuous flow suction. B) Pulsed injection with a simultaneous pulsed suction. Model B requires a fluidic actuator (e.g. a micro-compressor) turn on and off at the injection frequency. It would be very difficult to require a mechanical fluidic system to respond in a short time, in particular, to establish the required high pressure for injection within that time. Model B is thus infeasible.

Method A with continuous suction and pulsed injection appears to be a feasible model that is close to an achievable physical flow process. In Model A as illustrated in Fig. 7, the flow will be continuously pumped into a reservoir that will have increasing pressure when the injection is at its closed period. When the injection is open, the high pressure built in the reservoir will decrease by pushing the flow out as the injection jet. The pressure inside the reservoir will oscillate at the same frequency as the injection jet. Actually, the CC airfoil using aircraft engine bleed is similar to this process. The engine continuously withdraws a large amount of mass flow, which is a reservoir for the CC flow control injection. Model A with pulsed CFJ and continuous suction is adopted in this study.

As shown in Fig. 7, the present study simulates Model A with a pulsed velocity boundary condition (BC) at the CFJ injection duct (red) and a constant static pressure boundary condition at the CFJ suction duct (blue) for the continuous suction. The pulsed velocity varies following a square wave shown in Fig. 8, where “1” indicates the injection valve is open and “0” indicates it is closed. Since the micro-compressor is not included but represented by the boundary conditions in this study, the increase of total pressure ratio Γ due to the mass flow accumulation during the closed reservoir outlet is not simulated. In the present study, the time history of Γ is shown in Fig. 9. The solid lines in Fig. 9 is the simulated results during the injection showing the reservoir total pressure release. The dash lines are imaginary showing the total pressure rise during the injection closed period. The total pressure dynamic rise at injection closing is assumed to be symmetric to the total pressure dynamic decrease at the injection opening in this study. In reality, they may not be symmetric. However, this assumption is not expected to have a large effect on the results.

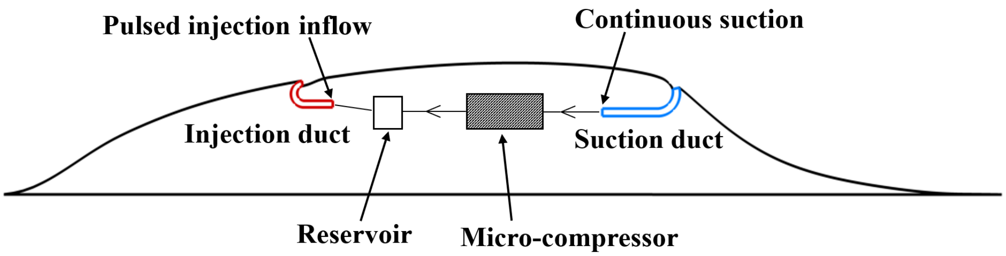

Figure 7: Numerical treatment of the pulsed CFJ hump

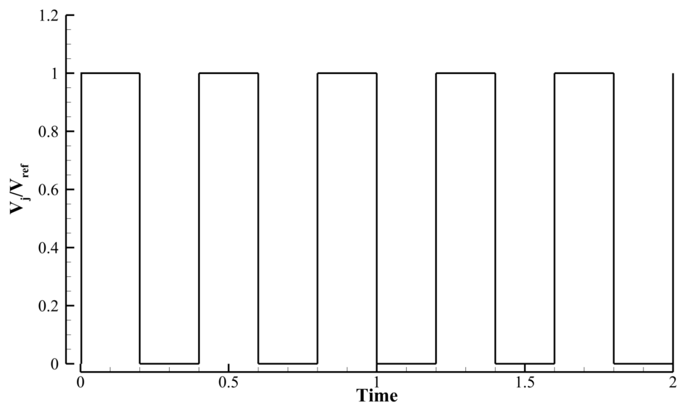

Figure 8: Sketch of the pulsed jet velocity variation

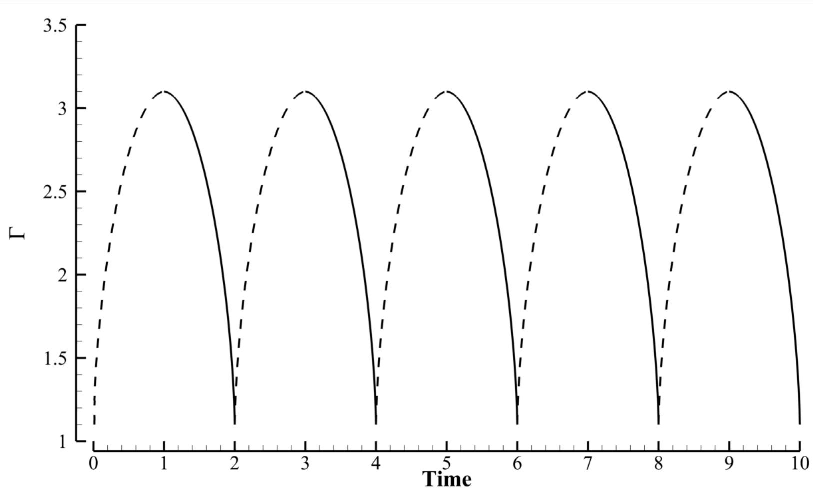

Figure 9: Time history of total pressure ratio in the present simulation

Since the total pressure ratio of micro-compressor varies periodically, the required power (P) will be calculated as a time averaged value within one pulsed period. The work done by the compressor dW within dt time can be expressed by:

$$dW = \frac{\dot{m}H_{t2}}{\eta}(\Gamma(t)^{\frac{\gamma-1}{\gamma}} - 1)dt \tag{4}$$

where $\dot{m}$ is mass flow rate of micro-compressor, H_{t2} is the total enthalpy at the suction slot, $\Gamma(t)$ is the total pressure ratio of the micro-compressor, and η is the pumping system efficiency, which is assumed 100% in this study to represent the required power.

Hence, the time-averaged power required ($\overline{P}$) for the pulsed jet can be defined:

$$\overline{P} = \frac{1}{T}\int_0^T dW = \frac{1}{T}\int_0^T \frac{\dot{m}H_{t2}}{\eta}(\Gamma(t)^{\frac{\gamma-1}{\gamma}} - 1)dt \tag{5}$$

where T is one pulsed period.

The time-averaged power coefficient ($\overline{P_c}$) is defined as:

$$\overline{P_c} = \frac{\overline{P}}{\frac{1}{2}\rho_{ref}U_{ref}^3 S_{ref}} \tag{6}$$

where ρ_{ref} and U_{ref} denote the reference density and velocity at the inlet, and S_{ref} is the reference area defined as the product of chord length and hump span in this study.

Similarly, the instant momentum coefficient ($C_\mu(t)$) and time-averaged momentum coefficient ($\overline{C_\mu}$) are expressed by Eq. (7) and Eq. (8) respectively.

$$C_\mu(t) = \frac{\dot{m}(t)V_j(t)}{\frac{1}{2}\rho_{ref}{U_{ref}}^2 S_{ref}} = \frac{A\rho(t)V_j(t)^2}{\frac{1}{2}\rho_{ref}{U_{ref}}^2 S_{ref}} \tag{7}$$

$$\overline{C_\mu} = \frac{1}{T}\int_0^T C_\mu(t)dt \tag{8}$$

where V_j is the mass-averaged injection velocity, $\rho(t)$ is the density of jet flow and A is the area of injection slot.

5 Results

This section compares the flow control effectiveness and energy efficiency between the steady CFJ and pulsed CFJ. Three cases are presented, a steady case and two pulsed cases at the reduced frequency of 0.74 and 1.67 used by [7, 63]. The pulsed CFJ cases are simulated at a duty cycle (DC) of 0.5. The presented cases all have the same CFJ configuration, which is adopted from the previous study [64]. The CFJ injection slot is located in the APG (adverse pressure gradient) region at 67.5%C with a slot-size of 0.5%C and suction duct is located at 90%C with a slot-size of 0.7%C. The goal is to compare the required P_c for all cases with the minimum C_μ that can achieve the attached flow. The results of pulsed CFJ are time averaged by 500 periods.

Fig. 10 shows the instantaneous pressure contours of the hump flow with steady and pulsed CFJ actuation. The steady CFJ case in Fig. 10 (a) shows that the pressure has a favorable pressure gradient till x/C=0.65 in the hump converging region and is followed by a pressure rise in the diffusion region. Pressure wave propagation is observed in Fig. 10 (b) and (c) excited by the pulsed actuation, and the low frequency case has a smaller number of pressure waves than the high frequency case. Fig. 11 compares the time-averaged Mach contours among the three cases. Full flow attachment is achieved by all the cases as indicated by the streamlines. The two pulsed CFJ cases require a 4.7% and 10.5% lower C_μ than the steady CFJ, respectively. Fig. 12 shows the time-averaged pressure coefficient (C_p) distributions. The pressure plateau observed in the baseline case due to flow separation is completely removed. All three cases achieve the same control effectiveness since their C_p are virtually identical.

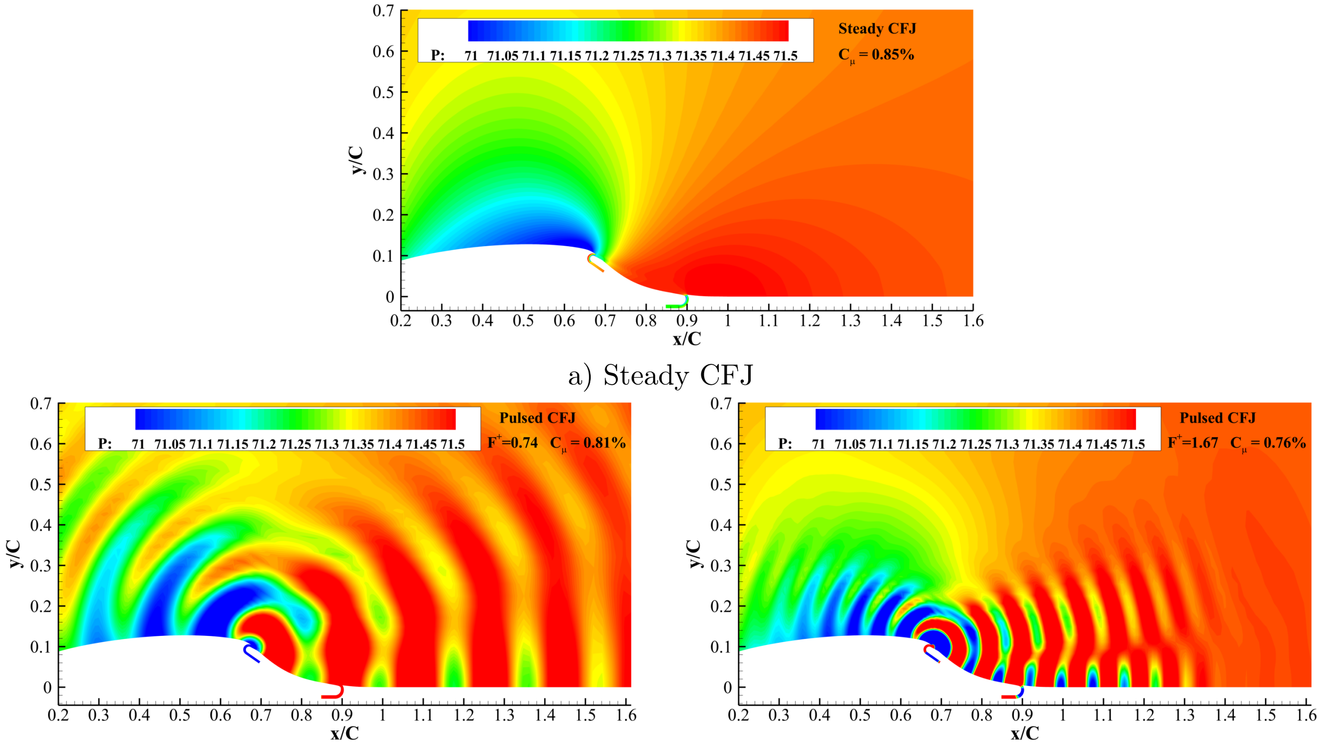

a) Steady CFJ

b) Pulsed CFJ, $F^+ = 0.74$

c) Pulsed CFJ, $F^+ = 1.67$

Figure 10: Instantaneous pressure contours of steady and pulsed CFJ cases.

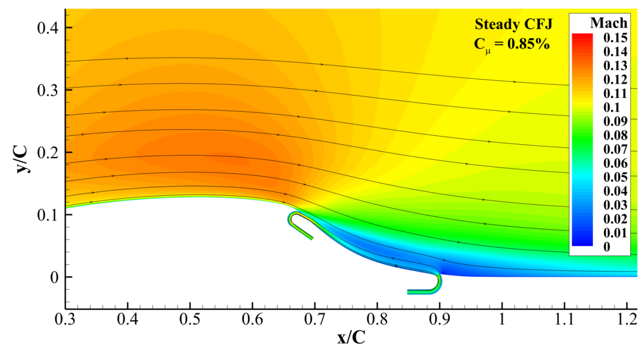

a) Steady CFJ

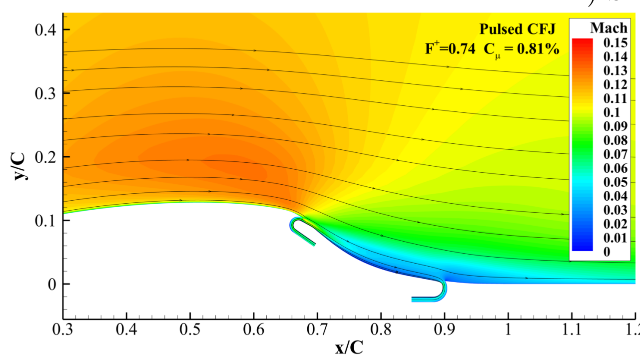

b) Pulsed CFJ, $F^+ = 0.74$

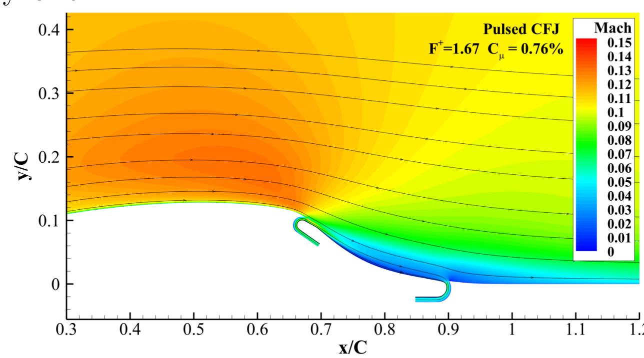

c) Pulsed CFJ, $F^+ = 1.67$

Figure 11: Time-averaged Mach number contours of steady and pulsed CFJ cases.

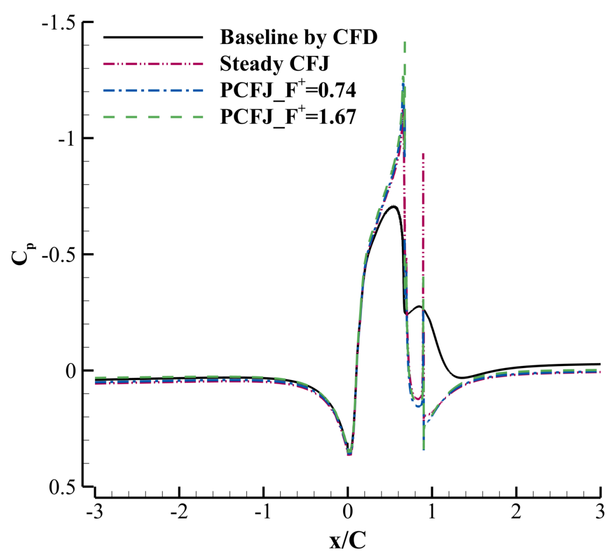

Figure 12: Comparisons of the time-averaged C_p distribution

Fig. 13 shows the time histories of the injection velocity, injection mass flow rate, injection jet momentum coefficient, and total pressure ratio (only half cycle when the jet is on) of the steady (dashed-dot line) and pulsed CFJ (solid and dashed lines). The pulsed injection is clearly indicated by the square wave of jet velocity. Fig. 13 (a) and (b) demonstrates that the pulsed CFJ cases have their peak velocity and peak mass flow rate higher than the steady jet, but the time-averaged mass flow rate is about 28% lower as presented in Table 1. The pulsed jet velocity is implemented by numerical boundary condition and is therefore a perfect square-wave. The mass flow rate is determined by the jet density and velocity that are varied non-linearly. Thus the mass flow rate does not have a square wave, in particular at the higher frequency. The high frequency case has a higher peak mass flow rate due to the increased density caused by the larger total pressure ratio Γ as shown in Fig. 13 (d). The total pressure ratio Γ of the pulsed CFJ is significantly higher than that of the steady case as indicated in Fig. 13 (d), which yields a power coefficient P_c about 5 and 8 times higher than that of the steady CFJ as given in Table 1. This is because delivering a certain mass flow in a shorter time period requires a much higher Γ, which exponentially increases the power coefficient P_c as indicated by Eq. (4) [64].

Overall, the comparison between pulsed CFJ and steady CFJ demonstrates that the pulsed jet requires lower mass flow rate to attach the flow, but it requires much higher power consumption.

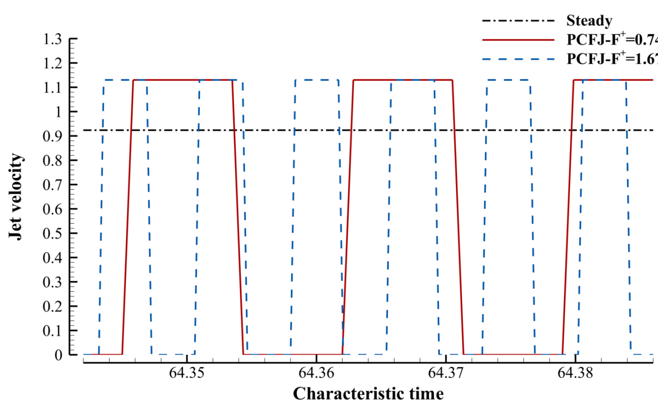

a) Injection velocity, V_j

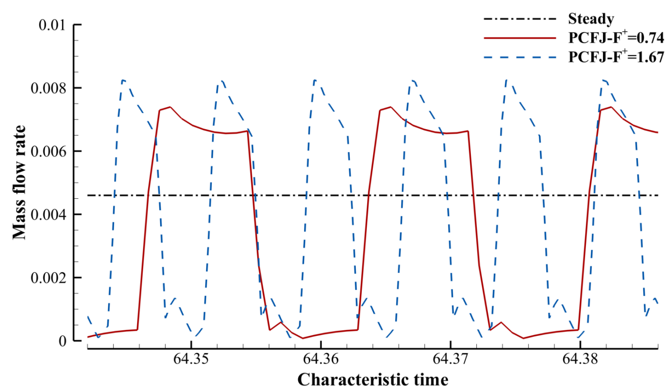

b) Mass flow rate, $\dot{m}$

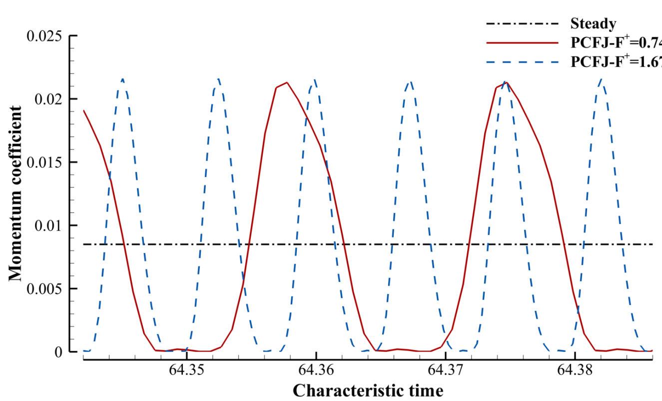

c) Momentum coefficient, C_μ

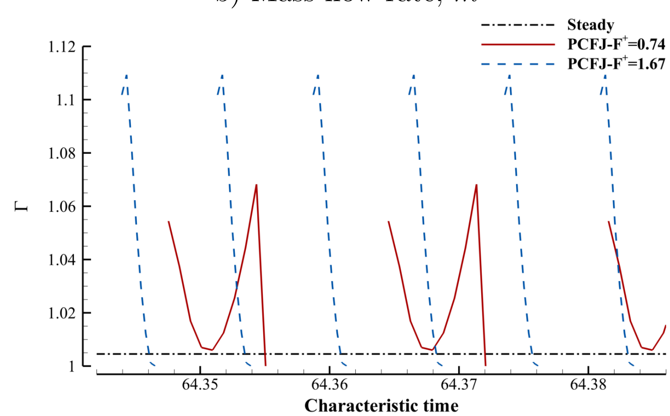

d) CFJ total pressure ratio Γ

Figure 13: Time histories of various jet parameters of pulsed and steady CFJ cases.

Table 1: Comparison of time-averaged jet parameters

Cases	F^+	Inj	Suc	$\overline{\dot{m}}$	$\overline{C_\mu}$	$\overline{P_c}$
Steady CFJ	-	67.5%C	90%C	0.0046	0.85%	0.003
Pulsed CFJ	0.74	67.5%C	90%C	0.0033	0.81%	0.014
Pulsed CFJ	1.67	67.5%C	90%C	0.0034	0.76%	0.024

Fig. 13 (d) indicates that the high frequency PCFJ case with F^+ of 1.67 has its total pressure ratio (Γ) vary in a mostly monotonic pattern as assumed in the PCFJ model in Fig. 9. The total pressure ratio Γ starts with a high value at the beginning of a jet-on period and gradually decreases until the end of the jet-on period. However, the Γ of the low frequency PCFJ case varies wavily with a peak right before the end of the jet-on period. Such a different Γ variation between the high and low frequency PCFJ cases can be explained by the instantaneous total pressure (p_t) and Mach number (M) contours inside the CFJ injection duct as shown in Figs. 14, 15, 16, and 17 for the low and high frequency case respectively. Fig. 14 (a) shows that at the beginning 1/10T period of the jet-on period, a high p_t occurs at the inlet of the injection duct. Since the rest of the flow inside the duct is still at low p_t status and the total pressure is quickly relieved as shown by the first drop in Fig. 13 (d). However, the flow at the exit of the injection slot is still at a low momentum state from the previous jet-off period (Fig. 14 and 15 (b) and (c)). It thus becomes a blockage for the flow pushed from the compressor outlet and increases the total pressure at the compressor outlet shown as the second peak in Fig. 13 (d). At the time 4/10T and 5/10T, the injection slot momentum is established by the push from the first wave of the high p_t. The injection duct blockage diminishes and the total pressure at the compressor outlet quickly drops at the end of the jet-on period.

For the high F^+ case, the high p_t flow from the last jet-on period still has a high momentum at the injection slot and no severe blockage is built at the exit as shown in Fig. 16 (a), (b), and (c). The total pressure at the compressor outlet thus monotonically decreases.

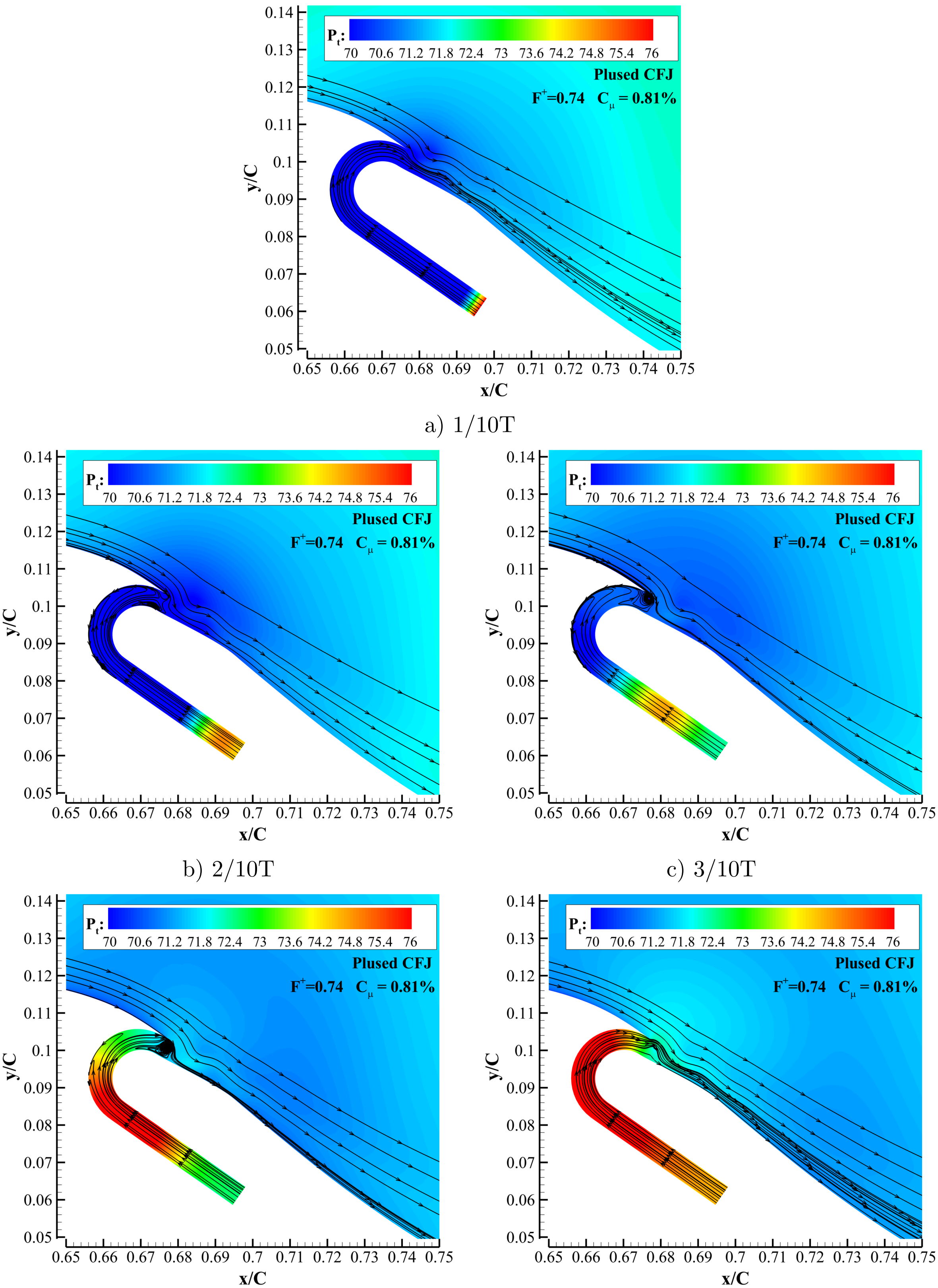

a) 1/10T

b) 2/10T

c) 3/10T

(d) 4/10T

(e) 5/10T

Figure 14: Instantaneous total pressure contours inside the injection duct for the jet-on period, C_μ=0.81%, F^+=0.74.

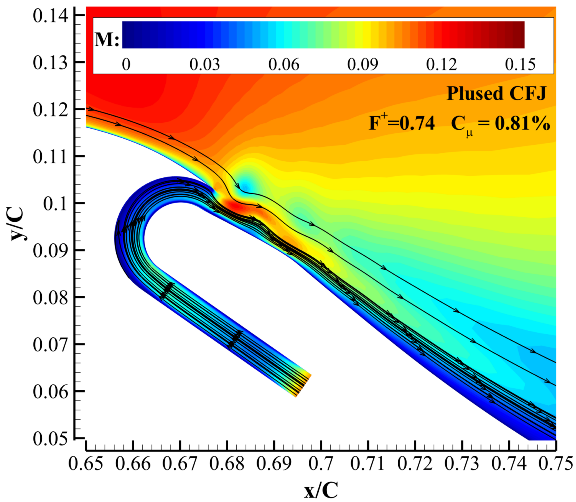

a) 1/10T

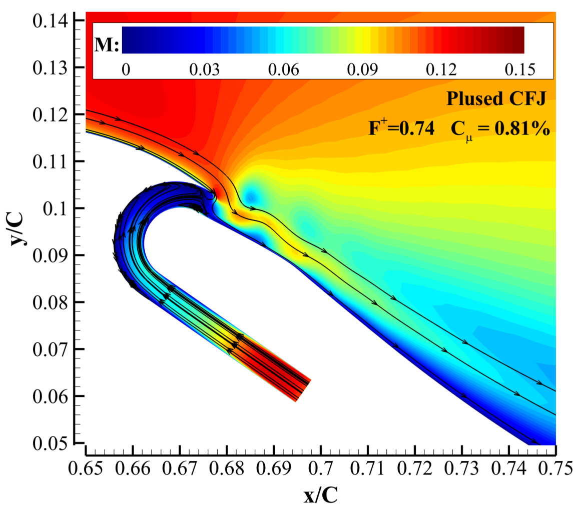

b) 2/10T

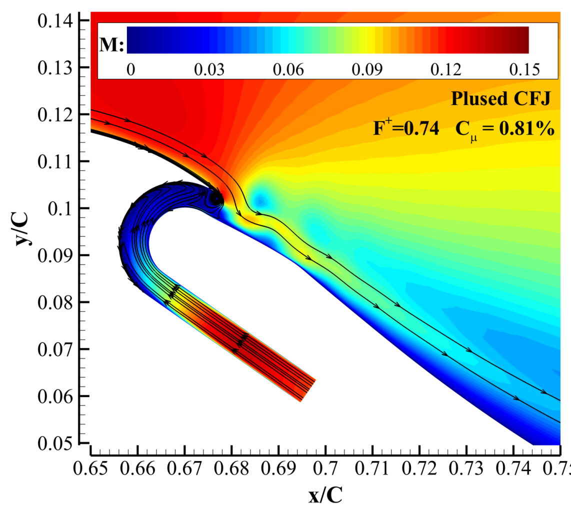

c) 3/10T

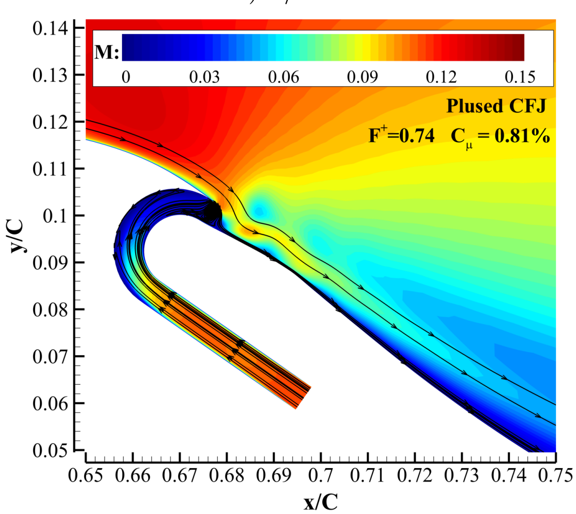

(d) 4/10T

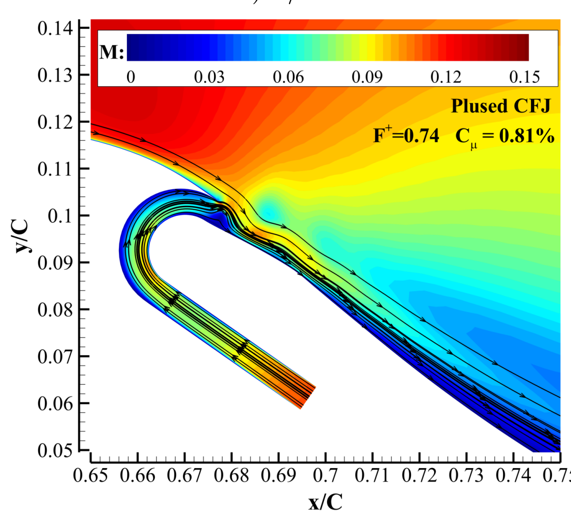

(e) 5/10T

Figure 15: Instantaneous Mach number (M) contours inside the injection duct for the jet-on period, C_μ=0.81%, F^+=0.74.

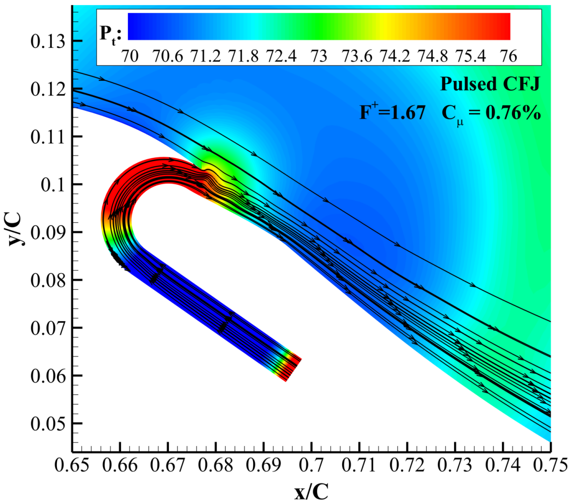

a) 1/10T

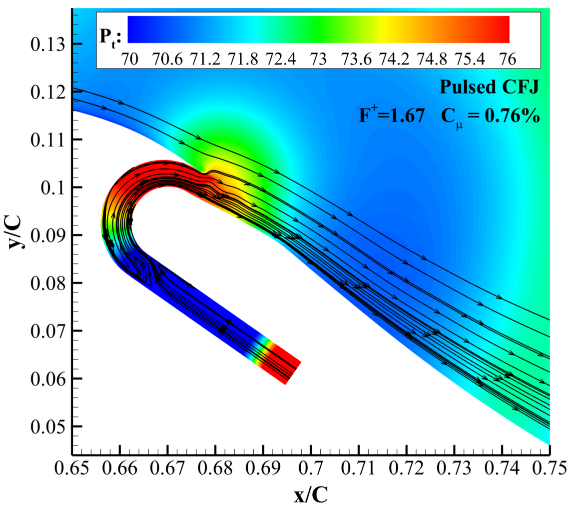

b) 2/10T

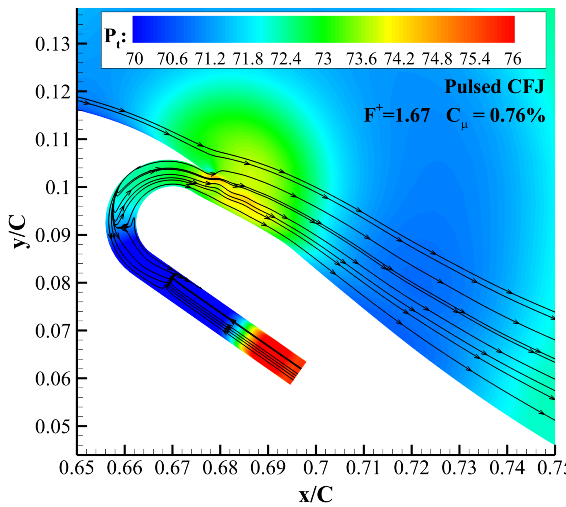

c) 3/10T

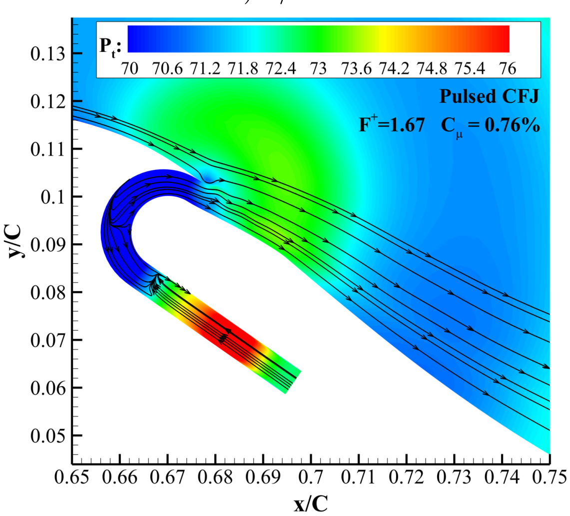

(d) 4/10T

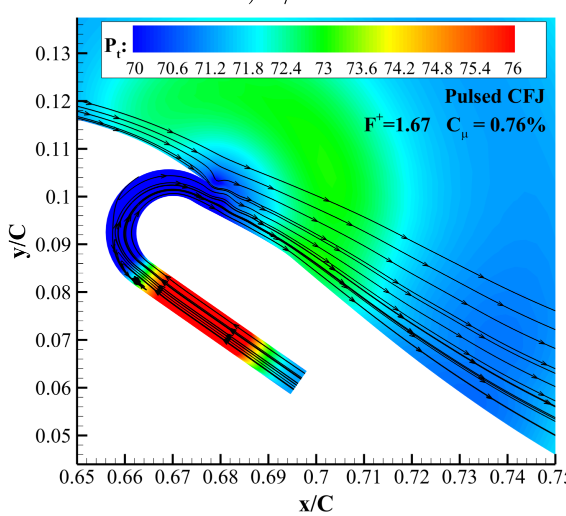

(e) 5/10T

Figure 16: Instantaneous total pressure contours inside the injection duct for the jet-on period, C_μ=0.76%, F^+=1.67.

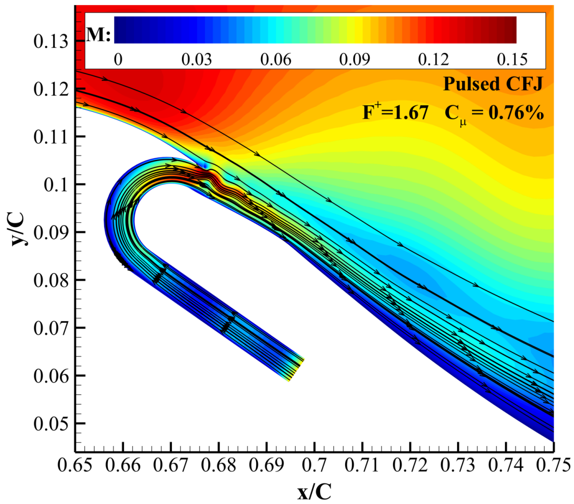

a) 1/10T

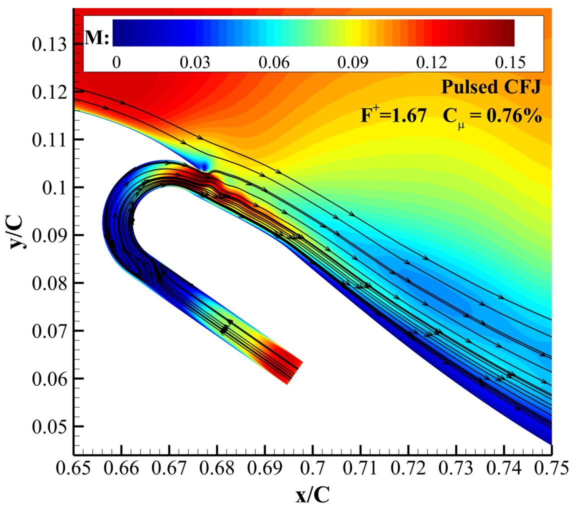

b) 2/10T

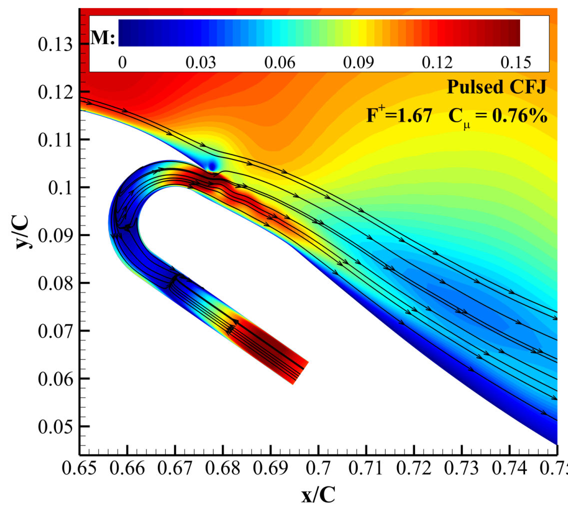

c) 3/10T

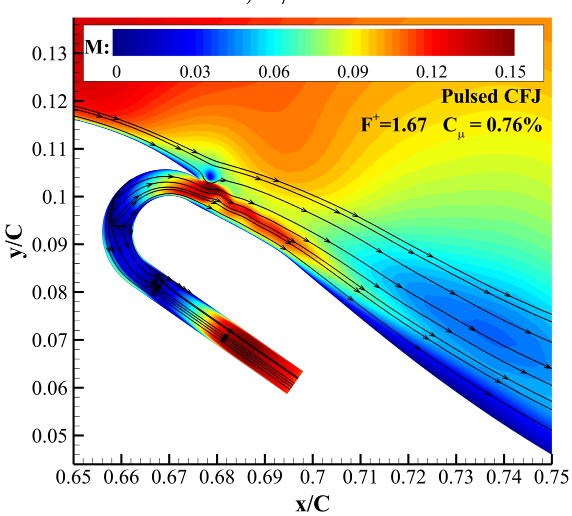

(d) 4/10T

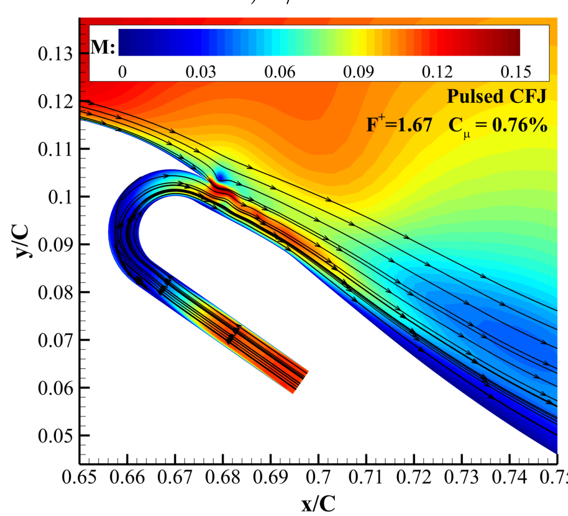

(e) 5/10T

Figure 17: Instantaneous Mach number (M) contours inside the injection duct for the jet-on period, C_μ=0.76%, F^+=1.67.

6 Conclusions

This paper numerically studies the control effectiveness and energy expenditure of pulsed Co-Flow Jet (PCFJ) applied on the widely used NASA hump. The 2D unsteady Reynolds averaged Navier-Stokes equations are solved for the simulations. An unsteady velocity boundary condition is developed for the in-house FASIP (Flow-Acoustics-Structure Interaction Package) CFD solver to simulate the pulsed CFJ. The pulsed jet simulation is validated with the NASA tested case actuated by a synthetic jet for the NASA hump flows. The predicted synthetic jet results are in good agreement with the experiment in terms of pressure coefficient (C_p) distributions. For the pulsed CFJ, a novel actuation model with continuous suction and pulsed injection is proposed to mimic the zero-net-mass-flux pulsing process and calculate the power consumption. The pulsed CFJ and steady CFJ (SCFJ) are compared for their control effectiveness and power consumption at their minimum momentum coefficient (C_μ) to fully attach the flow. The pulsed CFJ is simulated with two reduced frequencies (F^+) of 0.74 and 1.67. All the cases have identical CFJ injection and suction slot locations and sizes. Results show that the steady and pulsed CFJ cases have the similar control effectiveness as their C_p distributions are virtually overlapped. The PCFJ requires about 28% lower mass flow rate than that of the SCFJ. However, the PCFJ requires substantially higher power consumption due to significantly increased total pressure loss for pulsed jet actuation.

7 Acknowledgment

The authors would like to acknowledge the computing resource provided by the Center for Computational Sciences at the University of Miami.

Disclosure: The University of Miami and Dr. Gecheng Zha may receive royalties for future commercialization of the intellectual property used in this study.

References

[1] Gad-el-Hak, M., *Flow Control, Passive, Active, and Reactive Flow Management.* Cambridge University Press, 2000, DOI: 10.1017/CBO9780511529535.

[2] Prandtl, L. and Teitjens, O.G., *Applied hydro-and aeromechanics (Dover Books on Aeronautical Engineering)*, vol. 2. Dover Publications, 1934.

[3] Glezer, A. and Amitay, M., "Synthetic Jets," *Annual Review of Fluid Mechanics*, vol. 24, p. DOI: 10.1146/annurev.fluid.34.090501.094913, 2002.

[4] Jain, M. and Puranik, B. and Agrawal, A., "A numerical investigation of effects of cavity and orifice parameters on the characteristics of a synthetic jet flow," *Sensors and Actuators A: Physical*, vol. 165, no. 2, pp. 351–366, 2011, DOI: 10.1016/j.sna.2010.11.001.

[5] Mu, H. and Yan, Q. and Wei, W. and Sullivan, P.E., "Synthetic jet performance for different axisymmetric cavities analyzed with three-dimensional lattice-boltzmann method," *AIAA Journal*, vol. 56, no. 6, pp. 2499–2505, 2018, DOI: 10.2514/1.J056921.

[6] Kotapati, R.B. and Mittal, R. and Cattafesta Iii, L.N., "Numerical study of a transitional synthetic jet in quiescent external flow," *Journal of Fluid Mechanics*, vol. 581, pp. 287–321, 2007, DOI: 10.1017/S0022112007005642.

[7] Greenblatt, D., Paschal, K.B., Yao, C.S. and Harris, J., "Experimental Investigation of Separation Control Part 2: Zero Mass-flux Oscillatory Blowing," *AIAA journal*, vol. 44, no. 12, pp. 2831–2845, 2006, DOI: 10.2514/1.19324.

[8] Tang, G. and Agarwal, R.K., "Numerical Simulation of Flow Control Over NASA Hump with Uniform Blowing Jet and Synthetic Jet," in *2018 Flow Control Conference*, pp. AIAA 2018–4017, DOI: 10.2514/6.2018–4017, 2018.

[9] Thomas, F., Kozlov, A. and Corke, T. C., " Plasama Actuators for Cylinder Flow Control and Noise Reduction," *AIAA Journal* , vol. 46, pp. 1921–1931, 2008, DOI: 10.2514/1.27821.

[10] Zhang, Z., Wu, Y., Jia, M., Song, H., Sun, Z., Zong, H. and Li, Y., "The multichannel discharge plasma synthetic jet actuator," *Sensors and Actuators A: Physical*, vol. 253, pp. 112–117, 2017, DOI: .1016/j.sna.2016.11.011.

[11] Enloe, C.L. and Mangina, R.S. and Font, G.I., "Normalized electronegative species effects in the dielectric-barrier-discharge plasma actuator," *AIAA Journal*, vol. 54, no. 7, pp. 2061–2068, 2016, DOI: 10.2514/1.J054551.

[12] Shen, L. and Wen, C., "Leading edge vortex control on a delta wing with dielectric barrier discharge plasma actuators," *Applied Physics Letters*, vol. 110, no. 25, p. 251904, 2017, DOI: 10.1063/1.4989901.

[13] Sujar-Garrido, P., Benard, N., Moreau, E. and Bonnet, J.P., "Dielectric barrier discharge plasma actuator to control turbulent flow downstream of a backward-facing step," *Experiments in Fluids*, vol. 56, no. 4, p. 70, 2015, DOI: 10.1007/s00348-015-1939-1.

[14] Crowther, W. and Gomes, L., "An evaluation of the mass and power scaling of synthetic jet actuator flow control technology for civil transport aircraft applications," *Proceedings of the Institution of Mechanical Engineers, Part I: Journal of Systems and Control Engineering*, vol. 222, no. 5, pp. 357–372, 2008, DOI: 10.1243/09596518JSCE519.

[15] Gil, P. and Strzelczyk, P., "Performance and efficiency of loudspeaker driven synthetic jet actuator," *Experimental Thermal and Fluid Science*, vol. 76, pp. 163–174, 2016, DOI: 10.1016/j.expthermflusci.2016.03.020.

[16] Trávníček, Z. and Kordík, J., "Energetic efficiencies of synthetic jet actuators: Commentary on the article by gil and strzelczyk," *Experimental Thermal and Fluid Science*, vol. 98, pp. 121–123, 2018, DOI: 10.1016/j.expthermflusci.2018.05.025.

[17] Zito, J., Arnold, D., Houba, T., Soni, J., Durscher, R. and Roy, S., "Microscale dielectric barrier discharge plasma actuators: Performance characterization and numerical comparison." AIAA Paper 2012-3091, 43rd AIAA Plasmadynamics and Lasers Conference, New Orleans, Louisiana, June, 2012, DOI: 10.2514/6.2012-3091.

[18] Englar, R.J. and Williams, R. M., "Test Techniques for High Lift, Two Dimensional Airfoils with Boundary Layer and Circulation Control for Application to Rotary Wing Aircraft," *Canadian Aeronautics and Space Journal*, vol. 19, pp. 93–108, 1973.

[19] Englar, R. J. , "Circulation Control for High Lift and Drag Generation on STOL Aircraft," *Journal of Aircraft*, vol. 12, pp. 457–463, 1975, DOI: 10.2514/3.59824.

[20] Englar, R. J., "Circulation Control Pneumatic Aerodynamics: Blown Force and Moment Augmentation and Modifications; Past, Present and Future." AIAA 2000-2541, June 2000, DOI: 10.2514/6.2000-2541.

[21] Jones, G. S., “Pneumatic Flap Performance for a 2D Circulation Control Airfoil, Stedy & Pulsed.” *Applications of Circulation Control Technologies*, Chapter 7, p. 191-244, Vol. 214, Progress in Astronautics and Aeronautics, AIAA Book Series, Editors: Joslin, R. D. and Jones, G. S., 2006, DOI: 10.2514/4.866838.

[22] B. Nishri and I. Wygnanski, “Effects of periodic excitation on turbulent flow separation from a flap,” *AIAA journal*, vol. 36, no. 4, pp. 547–556, 1998.

[23] Seifert, A., Bachar, T., Koss, D., Shepshelovits, M. and Wygnanski, I., “ Oscillatory Blowing, a Tool to Delay Boundary Layer Separation,” *AIAA Journal* , vol. 31, pp. 2052–2060, 1993.

[24] A. Seifert, A. Darabi, and I. Wyganski, “Delay of airfoil stall by periodic excitation,” *Journal of aircraft*, vol. 33, no. 4, pp. 691–698, 1996.

[25] A. Seifert and L. Pack, “Oscillatory control of separation at high reynolds numbers,” *AIAA journal*, vol. 37, no. 9, pp. 1062–1071, 1999.

[26] Seifert, A. and Pack, L. G., “Active flow separation control on wall-mounted hump at high reynolds numbers,” *AIAA journal*, vol. 40, no. 7, pp. 1363–1372, 2002, DOI: 10.2514/2.1796.

[27] J. Bera, M. Michard, N. Grosjean, and G. Comte-Bellot, “Flow analysis of two-dimensional pulsed jets by particle image velocimetry,” *Experiments in fluids*, vol. 31, no. 5, pp. 519–532, 2001.

[28] G. Woo, T. Crittenden, and A. Glezer, “Transitory separation control over a stalled airfoil,” in *39th AIAA Fluid Dynamics Conference*, pp. AIAA 2009–4281, 2009.

[29] G. Woo, T. Crittenden, and A. Glezer, “Transitory control of a pitching airfoil using pulse combustion actuation,” in *4th Flow Control Conference*, pp. AIAA 2008–4324, 2008.

[30] C. Cagle, “A wind tunnel model to explore unsteady circulation control for general aviation applications,” in *22nd AIAA Aerodynamic Measurement Technology and Ground Testing Conference*, pp. AIAA 2002–3240, 2002.

[31] G. S. Jones, “Pneumatic flap performance for a 2d circulation control airfoil, stedy & pulsed,” *Applications of Circulation Control Technologies*, pp. 191–244, 2005.

[32] G. Jones, S. Viken, A. Washburn, L. Jenkins, and C. Cagle, “An active flow circulation controlled flap concept for general aviation aircraft applications,” in *1st Flow Control Conference*, pp. AIAA 2002–3157, 2002.

[33] Zha G., Carroll B.F., Paxton C.D., Conley C.A. and Wells A., “High-performance Airfoil Using Coflow Jet Flow Control,” *AIAA journal*, vol. 45, no. 8, pp. 2087–2090, 2007, DOI: 10.2514/1.20926.

[34] Lefebvre A., Dano B., Bartow W.B., Fronzo M.D. and Zha G., “Performance and Energy Expenditure of Coflow Jet Airfoil with Variation of Mach Number,” *Journal of Aircraft*, vol. 53, no. 6, pp. 1757–1767, 2016, DOI: 10.2514/1.C033113.

[35] Zha, G.-C., Gao, W. and Paxton, C.D., “Jet Effects on Co-Flow Jet Airfoil Performance.” AIAA Journal, Volum 45, pp 1222–1231, 2007, DOI: 10.2514/1.23995.

[36] Yang, Yunchao and Zha, Gecheng, “Super-Lift Coefficient of Active Flow Control Airfoil: What is the Limit?,” *AIAA Paper 2017-1693, AIAA SCITECH2017, 55th AIAA Aerospace Science Meeting, Grapevine, Texas*, p. 1693, 9-13 January 2017.

[37] Dano, B. P. E., Kirk, D. and Zha, G.-C., "Experimental Investigation of Jet Mixing Mechanism of Co-flow Jet Airfoil." AIAA-2010-4421, (5th AIAA Flow Control Conference, Chicago, IL), 28 Jun - 1 Jul 2010, DOI: 10.2514/6.2010-4421.

[38] Dano, B. P. E., Zha, G.-C. and Castillo, M., "Experimental Study of Co-Flow Jet Airfoil Performance Enhancement Using Micro Discreet Jets." AIAA Paper 2011-0941, 49th AIAA Aerospace Sciences Meeting, Orlando, FL,, 4-7 January 2011, DOI: 10.2514/6.2011-941.

[39] Lefebvre, A. and Zha, G.-C. , "Design of High Wing Loading Compact Electric Airplane Utilizing Co-Flow Jet Flow Control." AIAA Paper 2015-0772, AIAA SciTech2015: 53nd Aerospace Sciences Meeting, Kissimmee, FL, 5-9 Jan 2015, DOI: 10.2514/6.2015-0772.

[40] Lefebvre, A. and Dano, B. and Bartow, W. and Di Franzo, M. and Zha, G.-C., "Performance and Energy Expenditure of Co-Flow Jet Airfoil with Variation of Mach Number," *AIAA Journal of Aircraft*, vol. 53, pp. 1757–1767, 2016, DOI: 10.2514/1.C033113.

[41] Liu, Z.-X. and Zha, G.-C., "Transonic Airfoil Performance Enhancement Using Co-Flow Jet Active Flow Control." AIAA Paper 2016-3066, AIAA Aviation, June 13-17 2016, DOI: 10.2514/6.2016-3472.

[42] Lefebvre, A. and Zha, G.-C., "Trade Study of 3D Co-Flow Jet Wing for Cruise Performance." AIAA Paper 2016-0570, AIAA SCITECH2016, AIAA Aerospace Science Meeting, San Diego, CA, 4-8 January 2016, DOI: 10.2514/6.2016-0570.

[43] Zhang, J., Xu, K., Yang, Y., Ren, Y., Patel, P. and Zha, G.-C., "Aircraft Control Surfaces Using Co-flow Jet Active Flow Control Airfoil." AIAA Paper 2018-3067, 2018 Applied Aerodynamics Conference, Atlanta, Georgia, June 25-29, 2018, DOI: 10.2514/6.2018-3067.

[44] Xu, K. and Zha, G.-C., "Design of high specific speed mixed flow micro-compressor for co-flow jet actuators." GT2019-90980, IGTI Turbo Expo 2019, Phoenix, Arizona, USA, June 17 - 21, 2019, DOI: 10.1115/GT2019-90980.

[45] K. Xu and G. Zha, "Investigation of recirculating casing treatment for low-pressure ratio mixed-flow micro-compressor," in *Turbo Expo: Power for Land, Sea, and Air*, vol. 84195, p. V008T20A024, American Society of Mechanical Engineers, 2020.

[46] Spalart, P.R. and Allmaras, S.R. , "A One-equation Turbulence Model for Aerodynamic Flows." AIAA-92-0439, 30th Aerospace Sciences Meeting and Exhibit, Reno,NV,U.S.A., 06 January 1992 - 09 January 1992, DOI: 10.2514/6.1992-439.

[47] Zha, G.-C. and Bilgen, E., "Numerical Study of Three-dimensional Flows Using Unfactored Upwind-relaxation Sweeping Algorithm," *Journal of Computational Physics*, vol. 125, no. 2, pp. 425–433, 1996, DOI: 10.1006/jcph.1996.0104.

[48] Wang, B.-Y. and Haddoukessouni, B. and Levy, J. and Zha, G.-C., "Numerical Investigations of Injection Slot Size Effect on the Performance of Co-Flow Jet Airfoil," *Journal of Aircraft*, 2008, DOI: 10.2514/1.37441.

[49] Shen, Y.-Q. and Zha, G.-C., " Improved Seventh-Order WENO Scheme ." AIAA Paper 2010-1451, 48th AIAA Aerospace Sciences Meeting, Orlando, FL, Jan. 4-6, 2010, DOI: 10.2514/6.2010-1451.

[50] Zha, G.-C. and Shen, Y.-Q. and Wang, B., "An improved low diffusion E-CUSP upwind scheme ," *Journal of Computer & Fluids*, vol. 48, pp. 214–220, 2011, DOI: 10.1016/j.compfluid.2011.03.012.

[51] Shen, Y.-Q. and Zha, G.-C. and Wang, B.-Y., "Improvement of Stability and Accuracy for Weighted Essentially Nonoscillatory Scheme," *AIAA Journal*, vol. 47, pp. 331–344, 2009, DOI: 10.2514/1.37697.

[52] Shen, Y.-Q. and Zha, G.-C. and Chen, X.-Y., " High Order Conservative Differencing for Viscous Terms and the Application to Vortex-Induced Vibration Flows," *Journal of Computational Physics*, vol. 228(2), pp. 8283–8300, 2009. DOI: 10.1016/j.jcp.2009.08.004.

[53] Shen, Y.-Q. and Zha, G.-C. , " Improvement of the WENO Scheme Smoothness Estimator," *International Journal for Numerical Methods in Fluids*, vol. 64, 2010, DOI: 10.1002/fld.2186.

[54] Zha, G.-C. and Bilgen, E., "Numerical Solutions of Euler Equations by Using a New Flux Vector Splitting Scheme ," *International Journal for Numerical Methods in Fluids*, vol. 17, pp. 115–144, 1993, DOI: 10.1002/fld.1650170203.

[55] Chen, X. and Zha, G.-C., "Fully coupled fluid–structural interactions using an efficient high resolution upwind scheme," *Journal of Fluids and Structures*, vol. 20, no. 8, pp. 1105–1125, 2005, DOI: 10.1016/j.jfluidstructs.2005.02.011.

[56] Wang, B.-Y. and Zha, G.-C., "A General Sub-Domain Boundary Mapping Procedure For Structured Grid CFD Parallel Computation," *AIAA Journal of Aerospace Computing, Information, and Communication*, vol. 5, No.11, pp. 2084–2091, 2008, DOI: 10.2514/1.35498.

[57] Zha, G.-C and Paxton, C. and Conley, A. and Wells, A. and Carroll, B., "Effect of Injection Slot Size on High Performance Co-Flow Jet Airfoil," *AIAA Journal of Aircraft*, vol. 43, 2006, DOI: 10.2514/1.16999.

[58] Xu, K. and Zha, G.-C., "High Control Authority 3D Aircraft Control Surfaces Using Co-Flow Jet." AIAA Journal of Aircraft (2020), July 14, 2020. DOI: 10.2514/1.C035727, 2020.

[59] Rumsey, C., "2DWMH: 2D NASA Wall-Mounted Hump Separated Flow Validation Case." Turbulence Modeling Resource, turbmodels.larc.nasa.gov, 2003.

[60] Greenblatt, D., Paschal, K.B., Yao, C.S., Harris, J., Schaeffler, N.W. and Washburn, A.E., "Experimental Investigation of Separation Control Part 1: Baseline and Steady Suction," *AIAA journal*, vol. 44, no. 12, pp. 2820–2830, 2006, DOI: 514/1.13817.

[61] Xu, K. and Ren, Y. and Zha, G.-C., "Separation Control by Co-Flow Wall Jet," in *AIAA 2021 Aviation Forum, AIAA 2021-2946*, Virtual Event, June 2021, DOI: 10.2514/6.2021-2946.

[62] Naughton, J. W., Viken, S. and Greenblatt, D., "Skin Friction Measurements on the NASA Hump Model," *AIAA journal, DOI: 10.2514/1.14192*, vol. 44, no. 6, pp. 1255–1265, 2006.

[63] M. Koklu, "Steady and unsteady excitation of separated flow over the nasa hump model," in *2018 Flow Control Conference*, p. 4016, 2018.

[64] Xu K. and Ren Y. and Zha G., "Numerical Analysis of Energy Expenditure for Co-Flow Wall Jet Separation Control." Proceedings of AIAA 2022 SCITECH, San Diego, CA., January 2022.